

See discussions, stats, and author profiles for this publication at: <https://www.researchgate.net/publication/313411820>

Enhanced Photovoltaic Performance of Mesoscopic Perovskite Solar Cells by Controlling the Interaction Between $\text{CH}_3\text{NH}_3\text{PbI}_3$ Films and CsPbX_3 Perovskite Nanoparticles

Article in *The Journal of Physical Chemistry C* · February 2017

DOI: 10.1021/acs.jpcc.7b00861

CITATIONS

3

READS

346

7 authors, including:



Siraj Sidhik

Centro de Investigaciones en Optica

23 PUBLICATIONS 26 CITATIONS

SEE PROFILE



Diego Esparza

Autonomous University of Zacatecas

28 PUBLICATIONS 99 CITATIONS

SEE PROFILE



Tzarara López-Luke

Centro de Investigaciones en Optica

52 PUBLICATIONS 470 CITATIONS

SEE PROFILE




Iván Mora-Seró


Universitat Jaume I

165 PUBLICATIONS 13,256 CITATIONS

SEE PROFILE

Some of the authors of this publication are also working on these related projects:

 **Project** Simulación y Modelado de Materiales Semiconductores para Celdas Solares [View project](#)

 **Project** Perovskite solar cells [View project](#)

Enhanced Photovoltaic Performance of Mesoscopic Perovskite Solar Cells by Controlling the Interaction between $\text{CH}_3\text{NH}_3\text{PbI}_3$ Films and CsPbX_3 Perovskite Nanoparticles

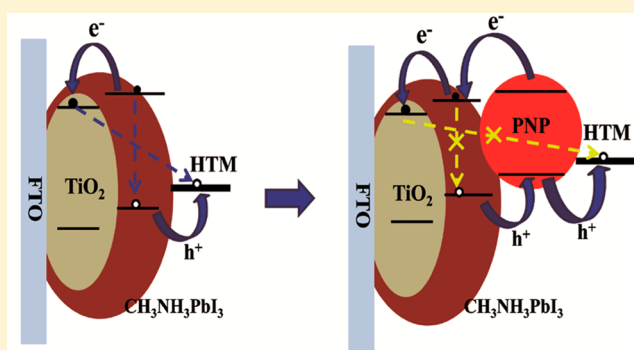
Siraj Sidhik,[†] Diego Esparza,[†] Alejandro Martínez-Benítez,[†] Tzarara Lopez-Luke,[†] Ramon Carriles,[†] Ivan Mora-Sero,[‡] and Elder de la Rosa^{*,†}

[†]Centro de Investigaciones en Optica, A.P. 1-948, Leon, Guanajuato 37150, Mexico

[‡]Photovoltaic and Optoelectronic Devices Group, Departament de Física, Universitat Jaume I, ES-12071 Castelló, Spain

Supporting Information

ABSTRACT: We report the incorporation of all-inorganic highly stable CsPbX_3 ($X = \text{I}, \text{Br}$) based perovskite nanoparticles (NPs) on top of a bulk $\text{CH}_3\text{NH}_3\text{PbI}_3$ perovskite thin film. This design utilizes the photogeneration ability of perovskite NPs and also improves the interfacial charge transport which happens to be a critical factor in deciding the photovoltaic performance of any solar cell device. With variation in the lead halide (PbX_2 , $X = \text{I}, \text{Br}, \text{Cl}$) content, the synthesized CsPbX_3 NPs shows tunable band-edge position and fluorescence characteristics. The interaction of all inorganic NPs with the bulk perovskite resulted in improved hole injection and electron blocking characteristics leading to enhanced light harvesting efficiency. The CsPbBr_3 and CsPbI_3 perovskite NPs were used for fabricating the bulk-NP structure due to their better absorption and valence band edge characteristics. The inclusion of CsPbI_3 NPs on top of the bulk perovskite showed a significant increment in the power conversion efficiency of 28%, in comparison with a reference sample without NPs, due to significant improvements in current density, open circuit voltage, and fill factor.



1. INTRODUCTION

Organic–inorganic perovskite based solar cells have attracted much attention in recent years because of their rapid increment in efficiency,^{1–4} high diffusion length,^{5–8} solution processable nature,^{9–12} excellent optical properties,^{13–16} and economic feasibility.^{17,18} The most recognized and widely used halide perovskite materials are the methylammonium lead halides ($\text{CH}_3\text{NH}_3\text{PbX}_3$, $X = \text{Br}, \text{Cl}, \text{I}$).^{19–21} These materials were used for the first time as sensitizers in dye-sensitized solar cells (DSSCs).²² To this date, a great amount of research has been carried out in the field of perovskite solar cells (PSCs) trying to improve the photoconversion efficiency (PCE), transport characteristics, morphology, hysteresis, and stability.^{4,23–34} Although, the PSCs with methylammonium lead halide have reached a maximum efficiency higher than 20%,³⁵ there is still scope for improvement in terms of better interfacial charge transport or inclusion of an additional absorbing layer mimicking the tandem configuration.

Semiconductor nanoparticles (NPs) have been broadly applied in different solar cell configuration, due to their high absorption coefficient and tunable energy levels.^{36–38} Very recently, M. Cha et al.,³⁹ reported an interface engineering method based on the incorporation of $\text{CH}_3\text{NH}_3\text{PbBr}_{3-x}\text{I}_x$ nanoparticles (NPs) between the perovskite film and hole-

transporting material (HTM) of a solar cell leading to improved hole extraction and then enhancing the PCE. However, such NPs suffer from poor stability due to the volatile organic part. Therefore, an all-inorganic NP structure is preferable. More recently, A. Swarnkar et al.,⁴⁰ reported the use of $\alpha\text{-CsPbI}_3$ for the fabrication of an all-inorganic perovskite NP photovoltaic cell and light emitting diode with long-term stability. These, all-inorganic perovskite NPs (CsPbX_3 , $X = \text{Cl}, \text{Br}, \text{and I}$) have shown good stability, high photoluminescence (PL) quantum yield, tunable bandgap and low excitation energy.^{41–45} Also, these NPs have similar processing requirements and lattice constants to that of bulk perovskite layers.⁴⁶ These points to the enormous potential of all inorganic perovskite NPs in improving the photovoltaic performance of bulk PSCs with higher stability.

In this paper, we report the incorporation of all-inorganic perovskite NPs on a bulk PSC. We found improved hole injection and electron blocking characteristics at the interface between the perovskite and HTM, leading to a significant increase in the PCE. A series of composition-tailored all-

Received: January 26, 2017

Revised: February 1, 2017

Published: February 6, 2017

inorganic perovskite NPs, (CsPbX_3 , $X = \text{Cl, Br, and I}$) were synthesized and characterized. CsPbBr_3 and CsPbI_3 NPs were incorporated between the bulk perovskite and HTM (spiro-MeOTAD), due to their favorable bandgap properties and washing characteristics. A notable increment in PCE of 28%, from 11.94% to 15.33%, was observed for this bulk perovskite/ CsPbI_3 NPs configuration in comparison to a $\text{CH}_3\text{NH}_3\text{PbI}_3$ /HTM device used as reference.

2. EXPERIMENTAL SECTION

2.1. Fabrication of Bulk Perovskite/ CsPbX_3 ($X = \text{I, Br}$) NP Device. *Synthesis of CsPbX_3 ($X = \text{I, Br, or Cl}$) Nanoparticles.* CsPbX_3 NPs were prepared following literature previously reported method¹⁷ takes advantage of the ionic nature of chemical bonds between the compounds, Cs^{2+} , Pb^{2+} , and X^- . The CsPbX_3 nanocrystals were obtained by reacting cesium oleate with lead(II) halide (PbX_2) in octadecene at a temperature of 170 °C. The Cs-oleate solution was prepared by mixing CsCO_3 (0.2 g, Sigma-Aldrich, 99.9%) with octadecene (10 mL, ODE, Sigma-Aldrich, 99%) and oleic acid (1 mL, OA, Sigma-Aldrich, 99%) in a 50 mL three-neck flask. The mixture was heated in the presence of nitrogen at 150 °C for complete solubilization of CsCO_3 and kept at 100 °C throughout the process. Further, a 1:1 molar ratio of OA and OLA with octadecene is added to the PbX_2 (0.376 mmol) for complete solubility and stabilization of synthesized nanocrystals. After complete solubilization, the PbX_2 mixture was heated to a temperature of 170 °C, to which the Cs-oleate solution (1 mL in ODE) is added instantly. The reaction took place so rapidly that the entire growth of nanocrystals occurred within 1–3 s. It is observed that, the size of nanocrystals could be tuned just by controlling the reaction temperature instead of the growth time. The obtained crude solution was cooled in an ice bath and the nanocrystals were separated by centrifugation. Finally, the nanocrystals were dispersed in anhydrous chlorobenzene for their incorporation into the PSCs.

Synthesis of $\text{CH}_3\text{NH}_3\text{PbBr}_3$ NPs. $\text{CH}_3\text{NH}_3\text{PbBr}_3$ NPs were synthesized using the LARP technique. $\text{CH}_3\text{NH}_3\text{PbBr}_3$ (0.16 mmol, Sigma-Aldrich (99.9%)) and PbBr_2 (0.2 mmol, Sigma-Aldrich (99%)) were dissolved in 5 mL of *N,N*-dimethylformamide (DMF). 100 μL of octadecene (Sigma-Aldrich, 98%) and 0.5 mL of oleic acid (Sigma-Aldrich, 98%) were further introduced into the above mixture to form the precursor solution. A 5 mL aliquot of toluene was taken in a three neck flask and stirred vigorously. Finally, 0.5 mL of the precursor solution was added dropwise into the stirring toluene. The color of the solution turned from clear to light green. After that, the colloidal solution was centrifuged at 5000 rpm for 10 min to obtain the precipitate. The precipitates were redissolved in 1 mL of hexane to obtain the colloidal NPs for the spectroscopic studies.

Fabrication of Bulk Perovskite Device. Solar cells with FTO/bl- TiO_2 / Li^+ -doped meso- TiO_2 /perovskite/spiro-MeOTAD/Ag-based mesoporous structure were prepared. Fluorine-doped tin oxide (FTO) coated glass (MTI, TEC-15) was patterned by etching with Zn powder and HCl diluted in distilled water. The etched substrate was further cleaned with detergent, diluted water and sonicated with absolute ethanol, absolute ethanol–acetone (50:50) in an ultrasonic bath for 15 min. The samples were UV–ozone (UVO) treated for 30 min. To prepare the TiO_2 blocking layer (bl- TiO_2), a mixture of titanium(IV) isopropoxide, acetylacetone, and anhydrous ethanol was deposited by spray pyrolysis at 450 °C.

Mesoporous TiO_2 was deposited on the blocking layer by spin coating the TiO_2 solution containing 1 g of TiO_2 paste (DSL 18-NRT, 20 nm average particle size) diluted in 5 g of anhydrous ethanol at 2000 rpm for 10 s. After the spin coating process, the substrates were dried at 100 °C for 10 min and then annealed at 450 °C for 30 min under dry air. Lithium doping of the mesoporous layer was accomplished by spin coating 0.03 M solution of bis(trifluoromethane)sulfonimide lithium salt (Li–TFSI) in acetonitrile. The solution was freshly prepared before the spin coating process in nitrogen atmosphere. 140 μL of the solution were loaded onto the substrate and spin coated at 3000 rpm for 10 s. The Li^+ doping was finished with a second calcination process at 450 °C for 30 min. After cooling down to room temperature, the samples were transferred to the nitrogen glovebox for perovskite deposition.

Fabrication of $\text{CH}_3\text{NH}_3\text{PbI}_3$ -Based Perovskite Film. PbI_2 (99.9%, Sigma-Aldrich), $\text{CH}_3\text{NH}_3\text{I}$ (Dyesol), and DMSO (99.9%, Sigma-Aldrich) (1:1:1 molar ratio) was mixed in 1 mL of anhydrous *N,N*-dimethylformamide (DMF, Sigma-Aldrich) at a temperature of 150 °C with stirring for 1 h to prepare the perovskite precursor solution. 80 μL of the perovskite solution were spin coated on the meso- TiO_2 at 5000 rpm for 20 s to form the perovskite film. During the spin coating process, 1.5 mL of anhydrous ethoxyethane (99.9%, Sigma-Aldrich) was instantly dropped exactly at the center of the substrate. The perovskite film was then transferred onto a hot plate, where it was heated at 100 °C for 3 min to form a dense $\text{CH}_3\text{NH}_3\text{PbI}_3$ film. The entire process was carried out inside a nitrogen-filled glovebox.

Fabrication of CsPbX_3 ($X = \text{I, Br, or Cl}$) Films. The CsPbX_3 NPs dispersed in chlorobenzene were spin coated onto the $\text{CH}_3\text{NH}_3\text{PbI}_3$ -based perovskite layer at 4500 rpm for 40 s. The obtained film was annealed at 100 °C for 5 min, resulting in the formation of perovskite/perovskite NP structure.

A spiro-MeOTAD solution was prepared consisting of 72.3 mg of spiro-MeOTAD (Merck), 28.8 μL of 4-*tert*-butylpyridine (TBP), 17.5 μL of lithium bis(trifluoromethane)sulfonimide (Li–TFSI) solution (520 mg Li–TFSI in 1 mL acetonitrile; Sigma-Aldrich, 99.8%), and 1 mL of chlorobenzene. 80 μL of the solution were spin-coated on the perovskite layer at 4000 rpm for 30 s. The solid state hole transporting layer was doped with different concentrations of tris(2-(1*H*-pyrazol-1-yl)-4-*tert*-butylpyridine)cobalt(III) tris[bis(trifluoromethane)sulfonimide] (FK209) complex, which was prepared by diluting 300 mg of the Co(III) complex in acetonitrile. Finally, a 60 nm thick Ag electrode was deposited by using a thermal evaporator at a constant evaporation rate of 2 nm/s.

2.2. Material Characterization. Scanning electron microscopy (SEM) images were obtained using a JSM-7800F microscope with an energy range of 1–5 keV. UV–vis absorption spectra were measured by diffuse reflectance in the range from 400 to 900 nm using an Agilent Technologies Cary Series UV–vis-NIR spectrophotometer (Cary 5000) and a 60 mm integrating sphere. The photoluminescence spectra of the NPs were recorded on an ACTON Spectrapro2300i photomultiplier tube. Current density curves were measured with a reference 600 Gamry potentiostat scanning from 0 to 1 V at 100 mV/s. The samples were illuminated with an Oriel Sol 3A solar simulator while measuring the current. The light intensity was adjusted by a KG-2 filter against a NREL calibrated Si solar cell in order to have one sun light intensity

(100 mW/cm²). incident photon current efficiency spectra were measured with a Newport, model74125, monochromator.

3. RESULTS AND DISCUSSION

A series of CsPbX₃ NPs were synthesized using the hot injection method with dry oleylamine (OLA) as the coligand and stabilizer, see Figure S1(a). This synthesis process is detailed in the Experimental Section. To study the morphology of nanoparticles, scanning transmission electron microscopy (STEM) images were acquired. Figure 1a shows a typical

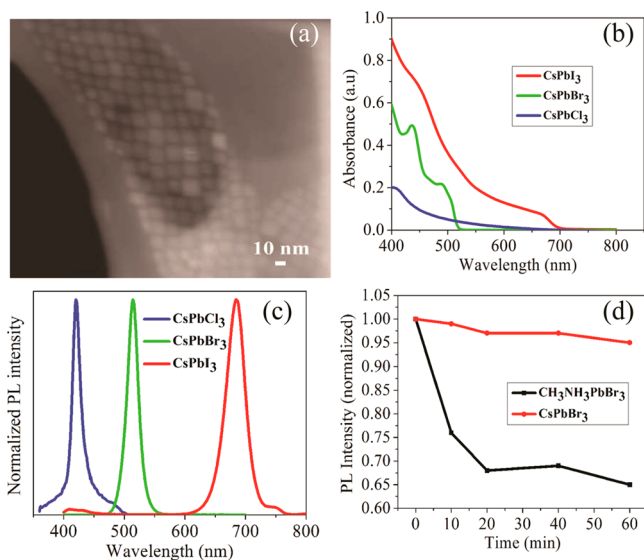


Figure 1. (a) Scanning transmission electron microscopy image of monodisperse CsPbI₃ nanocrystals. (b) Typical UV–vis absorption spectra for the colloidal NPs (CsPbX₃, X = I, Br, Cl). (c) Representative photoluminescence spectra, $\lambda_{\text{exc}} = 350$ nm for CsPbCl₃ samples and 400 nm for the rest. (d) Luminescence intensity changes with time of CH₃NH₃PbBr₃ and CsPbBr₃ NPs ($\lambda_{\text{em}} = 500$ nm) in solution under strong ultraviolet (UV) radiation.

micrography of the CsPbI₃ NPs; they have an average size of 9 nm with relatively good homogeneity. To determine the bandgap of synthesized CsPbX₃ NPs, UV–vis absorption spectroscopy was performed and it is shown in Figure 1b. The UV–visible spectra provided the gap between the valence band (VB) and conduction band (CB), by using the onset of absorption for each NPs. The bandgap (E_g) of CsPbI₃, CsPbBr₃, and CsPbCl₃ calculated using the τ_c plot was found to be 1.7, 2.2, and 3 eV, respectively. The size of all-inorganic perovskite NPs turns out to be an important factor in deciding the bandgap of synthesized nanocrystals. It is observed that

increasing the size of quantum dots leads to a decrement in the bandgap of the nanocrystals, which could affect the valence band and conduction band edges. The reported valence band edge for CsPbI₃ and CsPbBr₃ NPs without taking into account the quantum size effects are -5.4 and -5.56 eV.⁴⁷ The CB edges were calculated using the equation $\text{CB} = \text{VB} + E_g$, the resulting values were -3.7 and -3.4 eV for the NPs containing I and Br, respectively. The schematic energy band diagram for the synthesized CsPbX₃ (X = I, Br, Cl) NPs are depicted in Figure S1. Figure 1c shows the PL spectra of the three NPs. The emission peak is tuned by replacing the lead(II) halide (PbX₂, X = I, Br, and Cl) in the CsPbX₃ NP. The PL emission peaks were located at 685, 520, and 420 nm for X = I, Br, and Cl, respectively.

Photostability is still a challenge in designing NPs for application in optoelectronic devices like solar cells and light emitting diodes. The stability of all-inorganic CsPbBr₃ NPs was compared against hybrid CH₃NH₃PbBr₃ NPs which were synthesized using the ligand assisted reprecipitation (LARP) technique. Both samples were exposed to strong UV light for 60 min while monitoring their PL emission. It was observed that, the PL emission of the CsPbBr₃ NPs was highly stable even after prolonged exposure to UV radiation. A PL intensity decay of approximately 35% in the first 20 min of exposure was observed for the hybrid NPs compared to only 4% decay after 60 min of irradiation for the all-inorganic NPs,⁴⁸ see Figure 1d. This increased photostability of the all-inorganic perovskite NPs makes them an attractive candidate for applications in photovoltaic devices.^{44,49}

The CsPbI₃ and CsPbBr₃ NPs due to their better absorption and valence band edge characteristics were incorporated into a PSCs between the CH₃NH₃PbI₃ layer and the HTM (i.e., spiro-MeOTAD), to form a CH₃NH₃PbI₃/CsPbX₃-NPs/HTM device structure. The CsPbCl₃ NPs were not used because of the inappropriate valence band edge and absorption characteristics as shown in Figure S1. In general, the optimized perovskite structure consist of 30 nm thick TiO₂ compact layer on top of fluorine doped tin oxide (FTO), a 250 nm thick mesoporous layer, 300 nm thick perovskite capping layer, 200 nm spiro-MeOTAD film and 60 nm Ag contact which are depicted in the cross-sectional scanning electron microscopy (SEM) image in Figure 2a. Figure 2b shows the schematic representation of the fabrication of perovskite solar cell with the all-inorganic perovskite CsPbX₃ NPs.

The perovskite solution prepared by mixing PbI₂, CH₃NH₃I and DMSO in equimolar ratio is spin-coated on the meso-TiO₂ layer to form dark-brown perovskite film. During the spin coating process, 1.5 mL of anhydrous ethoxyethane was instantly dropped exactly at the center of the substrate. To obtain a perovskite film of high quality, the dropping time of

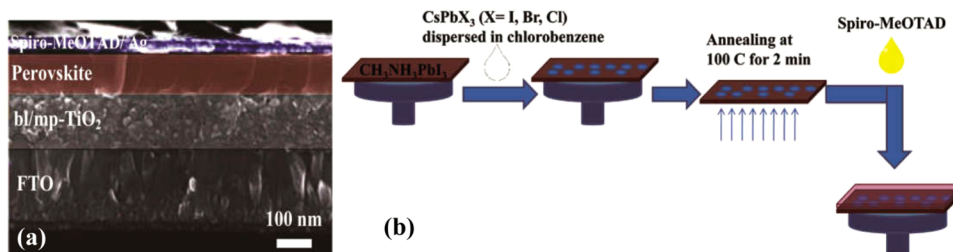


Figure 2. (a) High-resolution cross-section SEM image of a complete perovskite solar cell showing FTO, blocking/mesoporous TiO₂, smooth perovskite, HTM, and Ag contact. (b) Schematic representation of the fabrication process of perovskite solar cell with CsPbX₃ (X = I, Br, Cl) NPs.

nonpolar solvent on the spinning perovskite film should be controlled. It is observed that, the dropping time of 10 s results in a high quality perovskite film. A washing time of 10 s results in the formation of highly crystalline, pinhole free, homogeneous and uniform perovskite film, see Figure S2. Figure S2(a)-(c) shows the transformation from a needle like perovskite deposition into a uniform, better morphological and crystalline surface. More importantly, the crystal grains have grown and merged together with reduced gap region as evident in Figure S2(c). Some voids were observed on the surface of perovskite film for samples with washing time of 3 and 5 s. It may have occurred due to the fast washing of perovskite material with the nonpolar solvent, where the perovskite species get precipitated from the precursor solution and shrink leaving gaps within the film. It can be observed that, the increase in antisolvent washing time leads to drying of solvent and washing of the perovskite solution with the antisolvent (see Figure. S2(d)). The entire process was carried out inside nitrogen-filled glovebox. The all-inorganic CsPbX₃ (X = I and Br) based NPs dispersed in anhydrous chlorobenzene is spin coated on the CH₃NH₃PbI₃ film and annealed at a temperature of 100 °C for 2 min to prepare the perovskite-film/perovskite-NP configuration. The concentration of dispersed NPs turns out to be a critical factor that affects the performance of photovoltaic device; see Table S1. The spin-coating of 0.1 g/mL CsPbX₃ NPs for one time provides the best performance of the device. Increase in the concentration or number of spinning coating of NPs would open up new recombination points resulting in the decrease of photovoltaic performance. Also, much reduced concentration of dispersed NPs prevents excess carrier generation due to incorporated NPs on bulk perovskite. As a result, sufficient and optimized concentrations of NPs are necessary to keep alive the photogeneration effect of NPs and avoid recombination centers within the surface of perovskite film.

Parts a and b of Figure 3 show the top view SEM images of the perovskite film before and after the deposition of CsPbX₃

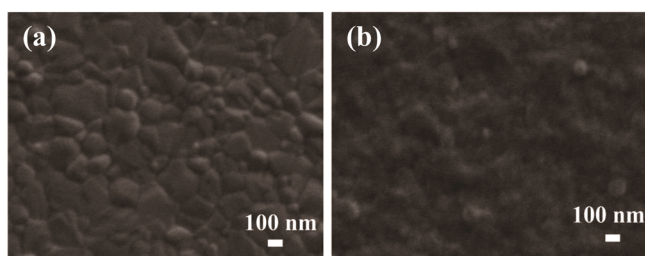


Figure 3. Top-view SEM images of CH₃NH₃PbI₃ layer, (a) before and (b) after deposition of CsPbX₃ NPs.

NPs. The bulk perovskite film formed before the incorporation of NPs showed clearly delimited grains. The introduction of NPs dispersed in chlorobenzene led to a smoother surface blurring the grain boundaries, see Figure 3b. Because of the small size of NPs (~9 nm), it is not possible to visualize them on top of perovskite film using SEM imaging. The UV-vis absorption spectra for PSC with and without the CsPbX₃ NPs are shown in Figure S3. The inclusion of a layer of NPs (CsPbI₃ and CsPbBr₃) on the bulk perovskite leads to an increment in light absorption as it could be expected from the addition of light absorbing material. The difference in level of absorption of two perovskite based devices incorporating CsPbI₃ and

CsPbBr₃ NPs can be attributed to the variation in concentration of NPs introduced on the bulk perovskite.

The current–voltage (*J–V*) curves for the best PSC device with CsPbBr₃ and CsPbI₃ NPs are shown in Figure 4a, and the

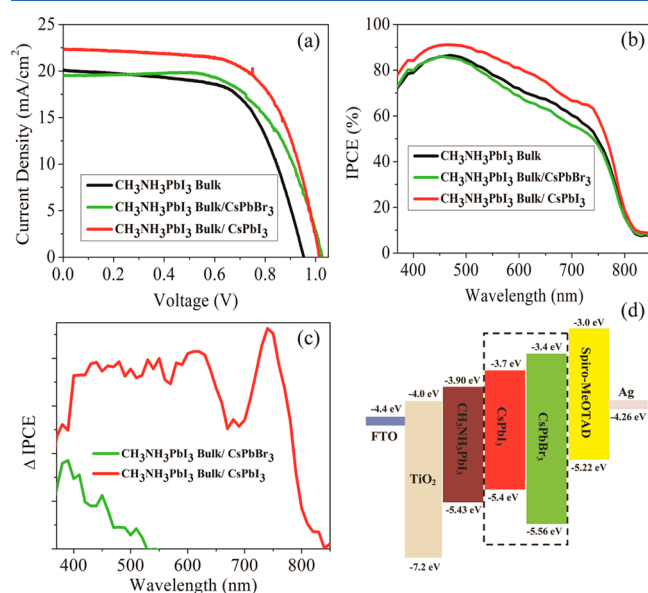


Figure 4. (a) *J–V* curves and (b) IPCE spectra of perovskite solar cells incorporated with CsPbX₃NPs. (c) Difference in IPCE curve of bulk perovskite and perovskite incorporated with CsPbX₃ NPs solar cells. (d) Energy band diagram of each material within the perovskite/CsPbX₃ structure, with energy levels given in eV showing the charge transport characteristics.

corresponding average photovoltaic parameters are indicated in Table 1. The photovoltaic performance of the device showed a significant change with the introduction of the CsPbX₃ NPs on top of bulk perovskite. A series of five cells for each configuration were fabricated and their photovoltaic characteristics were measured. The average PCE of typical mesoscopic CH₃NH₃PbI₃/HTM structure was found to be 11.94 ± 0.32%. When the all-inorganic CsPbX₃ (X = Br, I) based NPs were incorporated between the bulk perovskite and HTM, the average PCE for CH₃NH₃PbI₃(bulk)/CsPbBr₃ and CH₃NH₃PbI₃(bulk)/CsPbI₃ structure were 12.44 ± 0.45% and 15.33 ± 0.15%, respectively. The changes in the trend for each of the average photovoltaic parameters of *J*_{sc}, *V*_{oc} and FF is consistent with each best parameter; see Table 1.

The control cell (FTO/TiO₂/CH₃NH₃PbI₃/HTM) provides an average short current density (*J*_{sc}) of 20.03 mA/cm², open-circuit voltage (*V*_{oc}) of 0.95 V, fill factor (FF) of 62.90, yielding a PCE of 11.94%. The corresponding PCE of the device were little bit lower than those in other reports, but significant enough to extract interesting conclusions of the comparison between the reference sample and the perovskite(bulk)/perovskite NPs samples as the thin perovskite films is prepared in the same way in both configurations. The introduction of CsPbBr₃ NPs at the interface of bulk perovskite and HTM increased the photoconversion efficiency to 12.44% because of the increase in open circuit voltage from 0.95 to 1.02, while the current density and FF remains almost the same. Interestingly, the inclusion of CsPbI₃ NPs at the interface showed a much more pronounced effect with an increment of PCE by 28% when compared to the control cell. This device provided an increase in all the photovoltaic parameters, *J*_{sc} of 22.56 mA/

Table 1. Average Photovoltaic Parameters and Standard Deviations of Five Devices in Parallel under 1 Full Sun Irradiation for Perovskite and Perovskite(bulk)/Perovskite NPs Based Structures^a

device	J_{sc} (mA/cm ²)	V_{oc} (V)	FF	η_0 (%)
CH ₃ NH ₃ PbI ₃ (bulk)	20.03 ± 0.14	0.95 ± 0.02	62.90 ± 1.47	11.94 ± 0.32
CH ₃ NH ₃ PbI ₃ (bulk)/CsPbBr ₃	19.52 ± 0.11	1.02 ± 0.04	62.50 ± 1.87	12.44 ± 0.45
CH ₃ NH ₃ PbI ₃ (bulk)/CsPbI ₃	22.56 ± 0.12	1.014 ± 0.02	67.05 ± 1.53	15.33 ± 0.15

^aThe values inside bracket represent the best cell.

cm², V_{oc} of 1.014 V, and FF of 67.05, corresponding to an efficiency of 15.33%. All the photovoltaic parameters are significantly affected by the addition of perovskite NPs. Figure 4b shows the representative incident photon conversion efficiency (IPCE) obtained for the different cell configurations reported in Table 1 and Figure 4a. The IPCE increases in the order of CH₃NH₃PbI₃ bulk ≤ CH₃NH₃PbI₃ bulk/CsPbBr₃ < CH₃NH₃PbI₃ bulk/CsPbI₃NP. The integrated current density values calculated from IPCE is in good agreement with the measured current density. The differences in the IPCE curve, Δ IPCE, of the reference cell prepared with just perovskite film and cells with perovskite/perovskite-NPs structure are depicted in Figure 4c. The perovskite device containing CsPbBr₃ NPs showed a Δ IPCE at shorter wavelength which closely matches with the absorption spectrum of corresponding NPs, see Figure 1b. This proves the dominant photogeneration role of such perovskite NPs. However, the presence of CsPbI₃ NPs resulted in Δ IPCE extending from 400 to 800 nm matching the absorption spectrum of bulk perovskite film, see Figure S3. A dip in the Δ IPCE curve coincides with the photoluminescence (~670 nm) of CsPbI₃ NPs, which eliminates the photogeneration activity of NPs. However, on either sides of PL point of NPs, Δ IPCE shows a good increment. Such behavior confirms, in addition to the photogeneration ability, the dominant role to enhance the charge extraction due to the appropriate alignment of the energy levels.

According to the experimental results described above, the schematic energy level alignment of the perovskite/CsPbX₃ (X = I, Br) NPs is proposed and shown in Figure 4d. It helps to explain the differences in solar cell behavior observed for the devices analyzed in Table 1 that could arise from the following: (i) increase of light absorption when NPs are added with a corresponding impact in the photocurrent, see Figure 4a, as perovskite and NP band alignment favors the injection of the photogenerated electrons in the NPs into the perovskite layer while the photogenerated holes are injected into the HTM, see Figure 4d, allowing one to use the photoexcited carriers in the NPs to produce photocurrent; (ii) improvement of hole injection from the perovskite film into the HTM by an appropriate band alignment of the VB of the NPs for CsPbI₃, but not for CsPbBr₃, see Figure 4d, explaining the higher performance obtained when CsPbI₃ is used instead of CsPbBr₃;¹⁷ and (iii) electron blocking effect between perovskite and HTM, which has been reported as a main recombination pathway between electrons at the TiO₂ and holes at the *spiro*-OMeTAD²² caused by the presence of pinholes in the perovskite capping layer. Both NPs can produce this blocking effect due to the position of their CBs explaining the higher performance of devices with NPs even with the misalignment of the VB of CsPbBr₃ for an efficient hole injection, see Figure 4 d.

In order to get further insight on the interaction between the perovskite film and the perovskite NPs, steady-state photoluminescence (PL) measurements were recorded for an

excitation wavelength of 500 nm for samples with and without CsPbI₃ NPs and displayed in Figure 5. The dominant signal

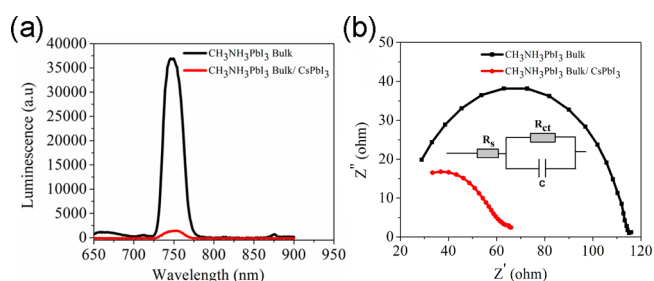


Figure 5. (a) Photoluminescence spectra of CH₃NH₃PbI₃ (control) and CH₃NH₃PbI₃ (bulk)/CsPbI₃ NPs based perovskite films. (b). Electrochemical impedance responses of PSCs with and without CsPbI₃ NPs measured at open circuit under AM1.5G simulated sunlight.

emitted is centered at 750 nm and is the result of bulk perovskite exciton recombination. The strong quenching on the PL of perovskite film suggests a faster hole extraction with the introduction of perovskite NPs, leading to reduced recombination in the bulk material. Such conclusion is consistent with the increase of J_{sc} (electron injection increase) and the significant enhancement of the IPCE, see Figure 4b.

Further, electrochemical impedance spectroscopy (EIS) measurements were carried out to understand the significant change in FF due to introduction of CsPbI₃ NPs on bulk perovskite. Figure 5b depicts the Nyquist spectra of reference bulk perovskite and bulk perovskite/CsPbI₃ NP structure under one sun illumination in a frequency range of 1 and 0.1 MHz with an equivalent circuit shown in the inset. In the equivalent circuit, R_s represents the series resistance due to FTO and external contact, R_{ct} represents the charge transfer resistance between CH₃NH₃PbI₃-HTM interface and C is the capacitance. It shows a semicircle resolved from the EIS spectra, which describes the behavior of charge transfer at the CH₃NH₃PbI₃ bulk-HTM interface. The intercept of semicircle on the real axis represents the series resistance (R_s). The R_s value is observed to be almost similar in both cases, thus neglecting its effect on the FF. However, a significant change in the value of R_{ct} is observed with the introduction of CsPbI₃ NPs at the interface of bulk perovskite and HTM. It indicates a more efficient hole transfer when compared to the reference cell due to appropriate band alignment of VB of the NPs for CsPbI₃. All these experimental results indicate that CsPbI₃ NPs at the interface of bulk perovskite and HTM can enhance charge separation leading to improved photocurrent, FF and PCE.

4. CONCLUSIONS

In summary, a mesoscopic perovskite solar cell embodied with all-inorganic CsPbX₃ (X = I, Br, Cl) NPs as light harvester and

interface engineering material is developed. Highly stable all-inorganic perovskite NPs were synthesized using hot injection method and were incorporated on the bulk perovskite film. Intensive characterization carried out to study the effect of NPs in the perovskite/perovskite NPs structure verifies the photogenerative role and interface regulating nature of the CsPbX₃nanocrystals. Hole transfer from bulk perovskite film into the HTM is observed to be favored by CsPbI₃ with appropriate VB edge properties and hindered by CsPbBr₃ due to lower VB edge. In addition, both types of NPs play the role of electron blocking layer. The increased light harvesting efficiency and improved interfacial characteristics with CsPbI₃ NPs leads to an increment in PCE of 28% with enhanced current density, open circuit voltage, and fill factor. This work would open up new possibilities and inspire new mechanisms for implementing productive interaction between halide perovskite films and nanoparticles.

■ ASSOCIATED CONTENT

● Supporting Information

The Supporting Information is available free of charge on the ACS Publications website at DOI: 10.1021/acs.jpcc.7b00861.

Photographs of the synthesized perovskite NPs under UV lamp, energy band diagram of the synthesized NPs, SEM images of perovskite film deposited on top of mesoporous titanium dioxide with solvent treatment for different delay times, UV–vis absorption spectra of CsPbX₃ NPs deposited on bulk perovskite film, photovoltaic parameters of PSCs fabricated by spin coating CsPbI₃ NPs with different concentrations and number of spin coating on the annealed CH₃NH₃PbI₃-based perovskite active layer (PDF)

■ AUTHOR INFORMATION

Corresponding Author

*(E.d.l.R.) E-mail: elder@cio.mx. Telephone: +52 (477) 441 42 00.

ORCID

Siraj Sidhik: 0000-0002-2097-2830

Ivan Mora-Sero: 0000-0003-2508-0994

Notes

The authors declare no competing financial interest.

■ ACKNOWLEDGMENTS

We acknowledge financial support from CONACYT through grant 259192, the UC-MEXUS program grant 00007 and the CEMIE-Solar (4002 and 4003) consortium. Two of the authors (Siraj Sidhik and Diego Esparza) acknowledge the Doctoral fellowship from SENER-CONACYT and CONACYT. We also thank Christian Albor and Carlos Juarez for technical support.

■ REFERENCES

- (1) Song, Z.; Wathage, S. C.; Phillips, A. B.; Heben, M. J. Pathways toward High-Performance Perovskite Solar Cells: Review of Recent Advances in Organo-Metal Halide Perovskites for Photovoltaic Applications. *J. Photonics Energy* **2016**, *6*, 022001–022001.
- (2) Liu, M.; Johnston, M. B.; Snaith, H. J. Efficient Planar Heterojunction Perovskite Solar Cells by Vapour Deposition. *Nature* **2013**, *501*, 395–398.
- (3) Nie, W.; Tsai, H.; Asadpour, R.; Blancon, J. C.; Neukirch, A. J.; Gupta, G.; Crochet, J. J.; Chhowalla, M.; Tretiak, S.; Alam, M. A.; et al.

High-Efficiency Solution-Processed Perovskite Solar Cells with Millimeter-Scale Grains. *Science* **2015**, *347*, 522–525.

(4) Saliba, M.; Matsui, T.; Seo, J. Y.; Domanski, K.; Correa-Baena, J. P.; Nazeeruddin, M. K.; Zakeeruddin, S. M.; Tress, W.; Abate, A.; Hagfeldt, A.; et al. Cesium-Containing Triple Cation Perovskite Solar Cells: Improved Stability, Reproducibility and High Efficiency. *Energy Environ. Sci.* **2016**, *9*, 1989–1997.

(5) Stranks, S. D.; Eperon, G. E.; Grancini, G.; Menelaou, C.; Alcocer, M. J.; Leijtens, T.; Herz, L. M.; Petrozza, A.; Snaith, H. J. Electron-Hole Diffusion Lengths Exceeding 1 Micrometer in an Organometal Trihalide Perovskite Absorber. *Science* **2013**, *342*, 341–344.

(6) Xie, F. X.; Su, H.; Mao, J.; Wong, K. S.; Choy, W. C. Evolution of Diffusion Length and Trap State Induced by Chloride in Perovskite Solar Cell. *J. Phys. Chem. C* **2016**, *120*, 21248–21253.

(7) Giordano, F.; Abate, A.; Correa Baena, J. P.; Saliba, M.; Matsui, T.; Im, S. H.; Zakeeruddin, S. M.; Nazeeruddin, M. K.; Hagfeldt, A.; Graetzel, M. Enhanced Electronic Properties in Mesoporous TiO₂ Via Lithium Doping for High-Efficiency Perovskite Solar Cells. *Nat. Commun.* **2016**, *7*, 10379.

(8) Zhumekenov, A. A.; Saidaminov, M. I.; Haque, M. A.; Alarousu, E.; Sarmah, S. P.; Murali, B.; Dursun, I.; Miao, X.-H.; Abdelhady, A. L.; Wu, T.; et al. Formamidinium Lead Halide Perovskite Crystals with Unprecedented Long Carrier Dynamics and Diffusion Length. *ACS Energy Lett.* **2016**, *1*, 32–37.

(9) Docampo, P.; Hanusch, F. C.; Stranks, S. D.; Döblinger, M.; Feckl, J. M.; Ehrensperger, M.; Minar, N. K.; Johnston, M. B.; Snaith, H. J.; Bein, T. Solution Deposition-Conversion for Planar Heterojunction Mixed Halide Perovskite Solar Cells. *Adv. Energy Mater.* **2014**, *4*, 1400355.

(10) Heo, J. H.; Lee, M. H.; Han, H. J.; Patil, B. R.; Yu, J. S.; Im, S. H. Highly Efficient Low Temperature Solution Processable Planar Type CH₃NH₃PbI₃ Perovskite Flexible Solar Cells. *J. Mater. Chem. A* **2016**, *4*, 1572–1578.

(11) Liu, X.; Tsai, K. W.; Zhu, Z.; Sun, Y.; Chueh, C. C.; Jen, A. K. Y. A Low-Temperature, Solution Processable Tin Oxide Electron-Transporting Layer Prepared by the Dual-Fuel Combustion Method for Efficient Perovskite Solar Cells. *Adv. Mater. Interfaces* **2016**, *3*, 1600122.

(12) Hanusch, F.; Petrus, M.; Docampo, P. Towards Optimum Solution-Processed Planar Heterojunction Perovskite Solar Cells. *Unconventional Thin Film Photovoltaics* **2016**, 32–56.

(13) D’Innocenzo, V.; Grancini, G.; Alcocer, M. J.; Kandada, A. R. S.; Stranks, S. D.; Lee, M. M.; Lanzani, G.; Snaith, H. J.; Petrozza, A. Excitons Versus Free Charges in Organo-Lead Tri-Halide Perovskites. *Nat. Commun.* **2014**, *5*, 3586.

(14) Ball, J. M.; Stranks, S. D.; Hörantner, M. T.; Hüttner, S.; Zhang, W.; Crossland, E. J.; Ramirez, I.; Riede, M.; Johnston, M. B.; Friend, R. H.; et al. Optical Properties and Limiting Photocurrent of Thin-Film Perovskite Solar Cells. *Energy Environ. Sci.* **2015**, *8*, 602–609.

(15) Quarti, C.; Mosconi, E.; Ball, J. M.; D’Innocenzo, V.; Tao, C.; Pathak, S.; Snaith, H. J.; Petrozza, A.; De Angelis, F. Structural and Optical Properties of Methylammonium Lead Iodide across the Tetragonal to Cubic Phase Transition: Implications for Perovskite Solar Cells. *Energy Environ. Sci.* **2016**, *9*, 155–163.

(16) Grancini, G.; Marras, S.; Prato, M.; Giannini, C.; Quarti, C.; De Angelis, F.; De Bastiani, M.; Eperon, G. E.; Snaith, H. J.; Manna, L.; et al. The Impact of the Crystallization Processes on the Structural and Optical Properties of Hybrid Perovskite Films for Photovoltaics. *J. Phys. Chem. Lett.* **2014**, *5*, 3836–3842.

(17) Chen, P.-Y.; Qi, J.; Klug, M. T.; Dang, X.; Hammond, P. T.; Belcher, A. M. Environmentally Responsible Fabrication of Efficient Perovskite Solar Cells from Recycled Car Batteries. *Energy Environ. Sci.* **2014**, *7*, 3659–3665.

(18) Jean, J.; Brown, P. R.; Jaffe, R. L.; Buonassisi, T.; Bulović, V. Pathways for Solar Photovoltaics. *Energy Environ. Sci.* **2015**, *8*, 1200–1219.

(19) Sheng, R.; Ho-Baillie, A.; Huang, S.; Chen, S.; Wen, X.; Hao, X.; Green, M. A. Methylammonium Lead Bromide Perovskite-Based Solar

Cells by Vapor-Assisted Deposition. *J. Phys. Chem. C* **2015**, *119*, 3545–3549.

(20) Colella, S.; Mosconi, E.; Fedeli, P.; Listorti, A.; Gazza, F.; Orlandi, F.; Ferro, P.; Besagni, T.; Rizzo, A.; Calestani, G.; et al. $\text{MaPb}_{1-x}\text{Cl}_x$ Mixed Halide Perovskite for Hybrid Solar Cells: The Role of Chloride as Dopant on the Transport and Structural Properties. *Chem. Mater.* **2013**, *25*, 4613–4618.

(21) Son, D.-Y.; Bae, K.-H.; Kim, H.-S.; Park, N.-G. Effects of Seed Layer on Growth of ZnO Nanorod and Performance of Perovskite Solar Cell. *J. Phys. Chem. C* **2015**, *119*, 10321–10328.

(22) Im, J. H.; Lee, C. R.; Lee, J. W.; Park, S. W.; Park, N. G. 6.5% Efficient Perovskite Quantum-Dot-Sensitized Solar Cell. *Nanoscale* **2011**, *3*, 4088–4093.

(23) Zuo, C.; Ding, L. An 80.11% FF Record Achieved for Perovskite Solar Cells by Using the NH_4Cl Additive. *Nanoscale* **2014**, *6*, 9935–9938.

(24) Zhou, H.; Chen, Q.; Li, G.; Luo, S.; Song, T.-b.; Duan, H.-S.; Hong, Z.; You, J.; Liu, Y.; Yang, Y. Interface Engineering of Highly Efficient Perovskite Solar Cells. *Science* **2014**, *345*, 542–546.

(25) Habisreutinger, S. N.; Leijtens, T.; Eperon, G. E.; Stranks, S. D.; Nicholas, R. J.; Snaith, H. J. Carbon Nanotube/Polymer Composites as a Highly Stable Hole Collection Layer in Perovskite Solar Cells. *Nano Lett.* **2014**, *14*, 5561–5568.

(26) Brenner, T. M.; Egger, D. A.; Kronik, L.; Hodes, G.; Cahen, D. Hybrid Organic-Inorganic Perovskites: Low-Cost Semiconductors with Intriguing Charge-Transport Properties. *Nature Reviews Materials* **2016**, *1*, 15007.

(27) Eperon, G. E.; Burlakov, V. M.; Docampo, P.; Goriely, A.; Snaith, H. J. Morphological Control for High Performance, Solution-Processed Planar Heterojunction Perovskite Solar Cells. *Adv. Funct. Mater.* **2014**, *24*, 151–157.

(28) Correa-Baena, J. P.; Anaya, M.; Lozano, G.; Tress, W.; Domanski, K.; Saliba, M.; Matsui, T.; Jacobsson, T. J.; Calvo, M. E.; Abate, A.; et al. Unbroken Perovskite: Interplay of Morphology, Electro-Optical Properties, and Ionic Movement. *Adv. Mater.* **2016**, *28*, 5031–5037.

(29) Zuo, L.; Dong, S.; De Marco, N.; Hsieh, Y.-T.; Bae, S.-H.; Sun, P.; Yang, Y. Morphology Evolution of High Efficiency Perovskite Solar Cells Via Vapor Induced Intermediate Phases. *J. Am. Chem. Soc.* **2016**, *138*, 15710–15716.

(30) Sanchez, R. S.; Gonzalez-Pedro, V.; Lee, J.-W.; Park, N.-G.; Kang, Y. S.; Mora-Sero, I.; Bisquert, J. Slow Dynamic Processes in Lead Halide Perovskite Solar Cells. Characteristic Times and Hysteresis. *J. Phys. Chem. Lett.* **2014**, *5*, 2357–2363.

(31) Ke, W.; Xiao, C.; Wang, C.; Saparov, B.; Duan, H. S.; Zhao, D.; Xiao, Z.; Schulz, P.; Harvey, S. P.; Liao, W.; et al. Employing Lead Thiocyanate Additive to Reduce the Hysteresis and Boost the Fill Factor of Planar Perovskite Solar Cells. *Adv. Mater.* **2016**, *28*, 5214–5221.

(32) Giuri, A.; Masi, S.; Colella, S.; Kovtun, A.; Dell'Elce, S.; Treossi, E.; Liscio, A.; Esposito Corcione, C.; Rizzo, A.; Listorti, A. Cooperative Effect of GO and Glucose on PEDOT: PSS for High V_{oc} and Hysteresis-Free Solution-Processed Perovskite Solar Cells. *Adv. Funct. Mater.* **2016**, *26*, 6985–6994.

(33) Dong, X.; Fang, X.; Lv, M.; Lin, B.; Zhang, S.; Ding, J.; Yuan, N. Improvement of the Humidity Stability of Organic-Inorganic Perovskite Solar Cells Using Ultrathin Al_2O_3 Layers Prepared by Atomic Layer Deposition. *J. Mater. Chem. A* **2015**, *3*, 5360–5367.

(34) Wang, Z.; McMeekin, D. P.; Sakai, N.; van Reenen, S.; Wojciechowski, K.; Patel, J. B.; Johnston, M. B.; Snaith, H. J. Efficient and Air-Stable Mixed-Cation Lead Mixed-Halide Perovskite Solar Cells with N-Doped Organic Electron Extraction Layers. *Adv. Mater.* **2017**, *29*, 1604186.

(35) Bi, D.; Yi, C.; Luo, J.; Décoppet, J.-D.; Zhang, F.; Zakeeruddin, S. M.; Li, X.; Hagfeldt, A.; Grätzel, M. Polymer-Templated Nucleation and Crystal Growth of Perovskite Films for Solar Cells with Efficiency Greater Than 21%. *Nature Energy* **2016**, *1*, 16142.

(36) Kongkanand, A.; Tvrđy, K.; Takechi, K.; Kuno, M.; Kamat, P. V. Quantum Dot Solar Cells. Tuning Photoresponse through Size and

Shape Control of CdSe-TiO₂ Architecture. *J. Am. Chem. Soc.* **2008**, *130*, 4007–4015.

(37) Esparza, D.; Zarazúa, I.; López-Luke, T.; Cerdán-Pasarán, A.; Sánchez-Solís, A.; Torres-Castro, A.; Mora-Sero, I.; De la Rosa, E. Effect of Different Sensitization Technique on the Photoconversion Efficiency of CdS Quantum Dot and CdSe Quantum Rod Sensitized TiO₂ Solar Cells. *J. Phys. Chem. C* **2015**, *119*, 13394–13403.

(38) Esparza, D.; Zarazúa, I.; López-Luke, T.; Carriles, R.; Torres-Castro, A.; De la Rosa, E. Photovoltaic Properties of Bi₂S₃ and CdS Quantum Dot Sensitized TiO₂ Solar Cells. *Electrochim. Acta* **2015**, *180*, 486–492.

(39) Cha, M.; Da, P.; Wang, J.; Wang, W.; Chen, Z.; Xiu, F.; Zheng, G.; Wang, Z.-S. Enhancing Perovskite Solar Cell Performance by Interface Engineering Using $\text{CH}_3\text{NH}_3\text{PbBr}_{0.9}\text{I}_{0.1}$ Quantum Dots. *J. Am. Chem. Soc.* **2016**, *138*, 8581–8587.

(40) Swarnkar, A.; Marshall, A. R.; Sanehira, E. M.; Chernomordik, B. D.; Moore, D. T.; Christians, J. A.; Chakrabarti, T.; Luther, J. M. Quantum Dot-Induced Phase Stabilization of α -CsPbI₃ Perovskite for High-Efficiency Photovoltaics. *Science* **2016**, *354*, 92–95.

(41) Li, X.; Wu, Y.; Zhang, S.; Cai, B.; Gu, Y.; Song, J.; Zeng, H. Quantum Dots: CsPbX₃ Quantum Dots for Lighting and Displays: Room-Temperature Synthesis, Photoluminescence Superiorities, Underlying Origins and White Light-Emitting Diodes (Adv. Funct. Mater. 15/2016). *Adv. Funct. Mater.* **2016**, *26*, 2584–2584.

(42) Akkerman, Q. A.; D'Innocenzo, V.; Accornero, S.; Scarpellini, A.; Petrozza, A.; Prato, M.; Manna, L. Tuning the Optical Properties of Cesium Lead Halide Perovskite Nanocrystals by Anion Exchange Reactions. *J. Am. Chem. Soc.* **2015**, *137*, 10276–10281.

(43) Ananthakumar, S.; Kumar, J. R.; Babu, S. M. Cesium Lead Halide (CsPbX₃, X = Cl, Br, I) Perovskite Quantum Dots-Synthesis, Properties, and Applications: A Review of Their Present Status. *J. Photonics Energy* **2016**, *6*, 042001–042001.

(44) Protesescu, L.; Yakunin, S.; Bodnarchuk, M. I.; Krieg, F.; Caputo, R.; Hendon, C. H.; Yang, R. X.; Walsh, A.; Kovalenko, M. V. Nanocrystals of Cesium Lead Halide Perovskites (CsPbX₃, X = Cl, Br, and I): Novel Optoelectronic Materials Showing Bright Emission with Wide Color Gamut. *Nano Lett.* **2015**, *15*, 3692–3696.

(45) Nedelcu, G.; Protesescu, L.; Yakunin, S.; Bodnarchuk, M. I.; Grotevent, M. J.; Kovalenko, M. V. Fast Anion-Exchange in Highly Luminescent Nanocrystals of Cesium Lead Halide Perovskites (CsPbX₃, X = Cl, Br, I). *Nano Lett.* **2015**, *15*, 5635–5640.

(46) Song, J.; Li, J.; Li, X.; Xu, L.; Dong, Y.; Zeng, H. Quantum Dot Light-Emitting Diodes Based on Inorganic Perovskite Cesium Lead Halides (CsPbX₃). *Adv. Mater.* **2015**, *27*, 7162–7167.

(47) Li, G.; Tan, Z.-K.; Di, D.; Lai, M. L.; Jiang, L.; Lim, J. H.-W.; Friend, R. H.; Greenham, N. C. Efficient Light-Emitting Diodes Based on Nanocrystalline Perovskite in a Dielectric Polymer Matrix. *Nano Lett.* **2015**, *15*, 2640–2644.

(48) Fang, H.-H.; Adjokatse, S.; Wei, H.; Yang, J.; Blake, G. R.; Huang, J.; Even, J.; Loi, M. A. Ultrahigh Sensitivity of Methylammonium Lead Tribromide Perovskite Single Crystals to Environmental Gases. *Science Advances* **2016**, *2*, e1600534.

(49) Matas Adams, A.; Marin-Beloqui, J. M.; Stoica, G.; Palomares, E. The Influence of the Mesoporous TiO₂ Scaffold on the Performance of Methyl Ammonium Lead Iodide (MAPI) Perovskite Solar Cells: Charge Injection, Charge Recombination and Solar Cell Efficiency Relationship. *J. Mater. Chem. A* **2015**, *3*, 22154–22161.